Research Article | Vol. 7, No. 12 | 1 Dec 2016 | BIOMEDICAL OPTICS EXPRESS 5092

Biomedical Optics EXPRESS

Characterization of transfer function, resolution and depth of field of a soft X-ray microscope applied to tomography enhancement by Wiener deconvolution

JOAQUÍN OTÓN,[1,*] EVA PEREIRO,[2] ANA J. PÉREZ-BERNÁ,[2] LAIA MILLACH,[3] CARLOS OSCAR S. SORZANO,[1] ROBERTO MARABINI,[4] AND JOSÉ M. CARAZO[1]

[1] *Centro Nacional de Biotecnología (CNB-CSIC), Cantoblanco, 28049, Madrid, Spain*
[2] *ALBA Synchrotron Light Source, Cerdanyola del Vallès, 08290, Barcelona, Spain*
[3] *Facultat de Biociències. Departament de Genètica i Microbiologia. UAB. Cerdanyola del Vallès, 08193, Barcelona, Spain*
[4] *Escuela Politecnica Superior, Univ. Autonoma de Madrid, Cantoblanco, 28049, Madrid, Spain*
[*] *joton@cnb.csic.es*
http://biocomp.cnb.csic.es

Abstract: Full field soft X-ray microscopy is becoming a powerful imaging technique to analyze whole cells preserved under cryo conditions. Images obtained in these X-ray microscopes can be combined by tomographic reconstruction to quantitatively estimate the three-dimensional (3D) distribution of absorption coefficients inside the cell. The impulse response of an imaging system is one of the factors that limits the quality of the X-ray microscope reconstructions. The main goal of this work is to experimentally measure the 3D impulse response and to assess the optical resolution and depth of field of the Mistral microscope at ALBA synchrotron (Barcelona, Spain). To this end we measure the microscope apparent transfer function (ATF) and we use it to design a deblurring Wiener filter, obtaining an increase in the image quality when applied to experimental datasets collected at ALBA.

© 2016 Optical Society of America

OCIS codes: (340.0340) X-ray optics; (040.7480) X-rays, soft X-rays; (110.7440) X-ray imaging; (180.7460) X-ray microscopy; (110.6960) Tomography; (110.4100) Modulation transfer function; (350.5730) Resolution; (100.1830) Deconvolution.

References and links

1. G. Schneider, P. Guttmann, S. Heim, S. Rehbein, F. Mueller, K. Nagashima, J. B. Heymann, W. G. Muller, J. G. McNally, and W. G. Müller, "Three-dimensional cellular ultrastructure resolved by X-ray microscopy," Nat. Methods **7**, 985–987 (2010).
2. J. Kirz, C. Jacobsen, and M. Howells, "Soft X-ray microscopes and their biological applications," Q. Rev. Biophys. **28**, 33–130 (1995).
3. M. Bertilson, O. von Hofsten, U. Vogt, A. Holmberg, and H. M. Hertz, "High-resolution computed tomography with a compact soft X-ray microscope," Opt. Express **17**, 11057–11065 (2009).
4. D. B. Carlson, J. Gelb, V. Palshin, and J. E. Evans, "Laboratory-based cryogenic soft X-ray tomography with correlative cryo-light and electron microscopy," Microsc. Microanal. **19**, 22–29 (2013).
5. W. Chao, P. Fischer, T. Tyliszczak, S. Rekawa, E. Anderson, and P. Naulleau, "Real space soft X-ray imaging at 10 nm spatial resolution," Opt. Express **20**, 9777–9783 (2012).
6. S. Rehbein, P. Guttmann, S. Werner, and G. Schneider, "Characterization of the resolving power and contrast transfer function of a transmission X-ray microscope with partially coherent illumination," Opt. Express **20**, 1–3 (2012).
7. J. Lehr, J. B. Sibarita, and J. M. Chassery, "Image restoration in X-ray microscopy: PSF determination and biological applications," in *IEEE transactions on image processing* **7**, 258–263 (1998).
8. D. Schäfer, M. Benk, K. Bergmann, T. Nisius, U. Wiesemann, and T. Wilhein, "Optical setup for tabletop soft X-ray microscopy using electrical discharge sources," Journal of Physics: Conference Series **186**, 012033 (2009).
9. Q. Yuan, K. Zhang, Y. Hong, W. Huang, K. Gao, Z. Wang, P. Zhu, J. Gelb, A. Tkachuk, B. Hornberger, M. Feser, W. Yun, and Z. Wu, "A 30 nm-resolution hard X-ray microscope with X-ray fluorescence mapping capability at BSRF," J. Synchrotron Radiat. **19**, 1021–1028 (2012).

#275785 http://dx.doi.org/10.1364/BOE.7.005092
Journal © 2016 Received 13 Sep 2016; revised 18 Oct 2016; accepted 22 Oct 2016; published 14 Nov 2016

Biomedical Optics EXPRESS

10. Y. S. Chu, J. M. Yi, F. De Carlo, Q. Shen, W.-K. Lee, H. J. Wu, C. H. L. H. L. Wang, J. Y. Wang, C. J. Liu, C. H. L. H. L. Wang, S. R. Wu, C. C. Chien, Y. Hwu, A. Tkachuk, W. Yun, M. Feser, K. S. Liang, C. S. Yang, J. H. Je, and G. Margaritondo, "Hard-X-ray microscopy with Fresnel zone plates reaches 40 nm Rayleigh resolution," Appl. Phys. Lett. **92**, 103119 (2008).
11. J. Chen, K. Gao, X. Ge, Z. Wang, K. Zhang, Y. Hong, Z. Pan, Z. Wu, P. Zhu, W. Yun, and Z. Wu, "Scattering imaging method in transmission X-ray microscopy," Opt. Lett. **38**, 2068–2070 (2013).
12. M. Uchida, G. McDermott, M. Wetzler, M. a. Le Gros, M. Myllys, C. Knoechel, A. E. Barron, and C. a. Larabell, "Soft X-ray tomography of phenotypic switching and the cellular response to antifungal peptoids in Candida albicans," P. Natl. Acad. Sci. USA **106**, 19375–19380 (2009).
13. E. M. H. Duke, M. Razi, A. Weston, P. Guttmann, S. Werner, K. Henzler, G. Schneider, S. A. Tooze, and L. M. Collinson, "Imaging endosomes and autophagosomes in whole mammalian cells using correlative cryo-fluorescence and cryo-soft X-ray microscopy (cryo-CLXM)," Ultramicroscopy **143**, 77–87 (2014).
14. C. Hagen, S. Werner, and S. Carregal-Romero, "Multimodal nanoparticles as alignment and correlation markers in fluorescence/soft X-ray cryo-microscopy/tomography of nucleoplasmic reticulum and apoptosis in mammalian cells," Ultramicroscopy **146**, 46–54 (2014).
15. K. C. Dent, C. Hagen, and K. Grünewald, "Critical step-by-step approaches toward correlative fluorescence/soft X-ray cryo-microscopy of adherent mammalian cells," Methods Cell Biol. **124**, 179–216 (2014).
16. J. J. Conesa, J. Otón, M. Chiappi, J. M. Carazo, E. Pereiro, F. J. Chichón, and J. L. Carrascosa, "Intracellular nanoparticles mass quantification by near-edge absorption soft X-ray nanotomography," Sci. Rep.**6**, 22354 (2016).
17. A. J. Pérez-Berná, M. J. Rodríguez, F. J. Chichón, M. F. Friesland, A. Sorrentino, J. L. Carrascosa, E. Pereiro, and P. Gastaminza, "Structural Changes In Cells Imaged by Soft X-Ray Cryo-Tomography During Hepatitis C Virus Infection," ACS Nano **10** (7), 6597–6611 (2016).
18. M. Chiappi, J. J. Conesa, E. Pereiro, C. O. S. Sorzano, M. J. Rodríguez, K. Henzler, G. Schneider, F. J. Chichón, and J. L. Carrascosa, "Cryo-soft X-ray tomography as a quantitative three-dimensional tool to model nanoparticle:cell interaction," J. Nanobiotechnology **14**, 15 (2016).
19. J. Oton, C. O. S. Sorzano, E. Pereiro, J. Cuenca-Alba, R. Navarro, J. M. Carazo, and R. Marabini, "Image formation in cellular X-ray microscopy," J. Struct. Biol. **178**, 29–37 (2012).
20. H. N. Chapman, "Phase-retrieval X-ray microscopy by Wigner-distribution deconvolution," Ultramicroscopy **66**, 153–172 (1996).
21. R. Burge, X.-C. Yuan, G. Morrison, P. Charalambous, M. Browne, and Z. An, "Incoherent imaging with the soft X-ray microscope," Ultramicroscopy **83**, 75–92 (2000).
22. E. Pereiro, J. Nicolás, S. Ferrer, and M. R. Howells, "A soft X-ray beamline for transmission X-ray microscopy at ALBA," J. Synchrotron Radiat. **16**, 505–512 (2009).
23. A. Sorrentino, J. Nicolás, R. Valcárcel, F. J. Chichón, M. Rosanes, J. Avila, A. Tkachuk, J. Irwin, S. Ferrer, and E. Pereiro, "MISTRAL: a transmission soft X-ray microscopy beamline for cryo nano-tomography of biological samples and magnetic domains imaging," J. Synchrotron Radiat. **22**, 1112–1117 (2015).
24. X. Zeng, F. Duewer, M. Feser, and C. Huang, "Ellipsoidal and parabolic glass capillaries as condensers for X-ray microscopes," Appl. Opt. **47**, 2376–2381 (2008).
25. D. Attwood, *Soft X-Rays and Extreme Ultraviolet Radiation: Principles and Applications* (Cambridge University, 2000).
26. W. Chao, B. D. Harteneck, J. A. Liddle, E. H. Anderson, and D. T. Attwood, "Soft X-ray microscopy at a spatial resolution better than 15 nm," Nature **435**, 1210–1213 (2005).
27. O. Mendoza-Yero, G. Minguez-Vega, R. Navarro, J. Lancis, and V. Climent, "PSF analysis of nanometric Fresnel zone plates," in "Proceeding of the EOS Topical Meeting on Diffractive Optics," 2428 (2010).
28. M. Born and E. Wolf, *Principles of Optics: Electromagnetic Theory of Propagation, Interference and Diffraction of Light* (Cambridge University, 1999).
29. J. W. Goodman, *Introduction to Fourier Optics* (McGraw-Hill, 1996).
30. C. Chang and T. Nakamura, "Partially coherent image formation theory for X-ray microscopy," in "Microscopy: Science, Technology, Applications and Education," 4th ed. M.-V. A. and D. J., eds. (Formatex Research Center, 2010), Chap. 3, pp. 1897–1904.
31. J. W. Goodman, *Statistical Optics*, A Wiley-Interscience publication (Wiley, 2000).
32. J. Otón, C. O. S. Sorzano, R. Marabini, E. Pereiro, and J. M. Carazo, "Measurement of the modulation transfer function of an X-ray microscope based on multiple Fourier orders analysis of a Siemens star," Opt. Express **23**, 9567 (2015).
33. H. Hopkins and P. Barham, "The influence of the condenser on microscopic resolution," Proceedings of the Physical Society Section B **63**, 737 (1950).
34. J. Oton, C. O. S. Sorzano, F. J. Chichón, J. L. Carrascosa, J. M. Carazo, and R. Marabini, "Soft X-ray Tomography Imaging for Biological Samples," in "Computational Methods for Three-Dimensional Microscopy Reconstruction," (2014), Chap. 8, p. 260.
35. I. G. Kazantsev, J. Klukowska, G. T. Herman, and L. Cernetic, "Fully three-dimensional defocus-gradient corrected backprojection in cryoelectron microscopy," Ultramicroscopy **110**, 1128–1142 (2010).
36. B. Gunturk, "Fundamentals of Image Restoration," in "Image Restoration: Fundamentals and Advances," B. K. Gunturk; and X. Li, eds. (CRC, 2012), pp. 25–62.

Biomedical Optics EXPRESS

37. J. Frank, *Three Dimensional Electron Microscopy of Macromolecular Assemblies* (Oxford University, 2006).
38. S. Gabarda and G. Cristóbal, "Blind image quality assessment through anisotropy," J. Opt. Soc. Am. A Op.t Image Sci. Vis. **24**, B42–B51 (2007).

1. Introduction

Full field soft X-ray tomography (SXT) refers to an emerging microscopy technique in which photons of wavelengths of a few nanometers are used to obtain images of objects of interest. Applied to biology, we refer to cryo-microscopes imaging whole cells at resolutions in the order of 50 nm and lower [1]. The contrast in these images can be relatively higher than in electron tomography, specially if photons with energy in the so called water window are used (between 284 and 543 eV) [2]. In this situation, images are formed mostly by absorption, being typical absorption values for biological specimens (carbon) an order of magnitude greater than the one of water (oxygen). Furthermore, these 2D image projections can be combined to obtain a quantitative estimation of the 3D structure of the cell by tomographic reconstruction techniques. This kind of microscopes needs a high photon flux, typical of synchrotron facilities, as can be found in ALBA (Spain), HZB-Bessy II (Germany), Diamond (UK) or ALS (US). Recently, the use of soft X-rays emitted from laser-produced plasmas rather than synchrotron radiation is becoming more popular [3, 4].

In order to characterize the X-ray microscope optical resolution, the impulse response function needs to be measured. To achieve this goal, several methods have been proposed based on: qualitative assessment [5, 6], specific contrast decay [7–9] and Rayleigh criteria [10, 11]. We have favoured this last one because it is obtained using parameters related with the microscope instead of visual inspection or a pure mathematical definition. Moreover, if these impulse response profiles are acquired along the optical axis at different defocus positions, it is possible to characterize the depth of field (DOF) of the microscope.

Most work performed on SXT microscopes addresses samples a few microns thick [4, 12–18]. Depending on the ratio between the sample thickness and the DOF, standard reconstruction algorithms introduce different artifacts which can be better estimated once the experimental DOF is known [19]. Even if the specimen is fully in focus, images are not perfect projections but they are blurred by the microscope impulse response. Although image deblurring by deconvolution is a well-known tool in image processing and, in fact, it has already been applied in scanning transmission X-ray microscopy [20, 21], this step has never been used in SXT before. Here, taking into account the experimental impulse response, we apply deconvolution techniques to experimental data.

In this work, we introduce the definitions of the apparent point spread function (APSF) and pseudo-apparent point spread function (PAPSF) that allow for the analysis of the impulse response of an optical system. Both functions are derived from the apparent transfer function (ATF). We provide the first experimental characterization of these profiles for the typical optical schemes used at the Mistral microscope, at ALBA synchrotron (Barcelona) [22, 23]. Using the experimental PAPSF 3D distribution, we calculate the Rayleigh resolution and depth of field of the microscope. Finally, we design a Wiener deconvolution filter which, once applied to experimental image projections prior to 3D reconstruction, results in an quality increase in the final tomograms.

2. Methods

In this section we describe a transmission X-ray microscope and the different magnitudes needed to characterize the optical system response. When these magnitudes cannot be directly measured we suggest and justify how to derive them from alternative measurements.

Biomedical Optics EXPRESS

2.1. Microscope optical system

The typical optical scheme of a full field transmission X-ray microscope is shown in Fig. 1. It is composed by both a condenser and objective lenses. The latest microscopes make use of achromatic single-bounce ellipsoidal glass capillaries as condensers [24]. In the case of objective lenses, Fresnel zone plates (FZP) are used [25]. These FZP are rotationally symmetric diffractive gratings, composed by radially decreasing width rings. The spatial resolution is intrinsically related to the width of the last ring which, at present, can reach up to 15 nm resolution [26]. Theoretical expressions that characterize the optics of an X-ray microscope are easily found in the literature [25, 27]. However, the manufacturing of these two kind of lenses is a rather complicated microfabrication process, so the final lenses will be an approximation to the ideal ones. Additionally, glass capillaries and FZPs are not the only optical elements used in these microscopes and other elements, as beam central stoppers, also take part in the scheme. As the FZP is a diffractive element, its zero order takes 25% of the incident energy, behaving this direct light as background noise in the projection. Therefore, this inefficient fraction of energy is removed by placing a central stopper just before the capillary condenser. The light source, usually the monochromator exit slit, is imaged by the condenser onto the sample plane in a scheme known as *critical illumination* [28] and, in general, the beam underfills the sample, problem that is overcome by wobbling the capillary.

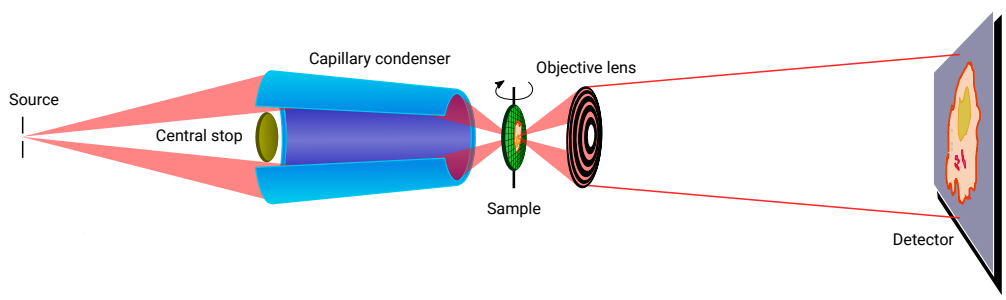

Fig. 1. Optical system scheme of a full field transmission X-ray microscope. The exit slit of a monochromator used to select the proper photon energy acts as light source. Beam is then condensed by an ellipsoidal glass capillary onto the sample plane, while a central stopper blocks the center part of the beam that is not reflected by the capillary. Finally, images are obtained by FZP objective lens.

In the case of the Mistral full-field transmission X-ray microscope, which was built by Xradia Inc. (now Zeiss), the single bounce glass capillary condenser is characterized by a length of 100 mm, with inner entrance and exit diameters of 1.82 and 0.58 mm, respectively, and works as a single reflection achromatic lens with a focal length of 10.05 mm. The exit slit of the monochromator is imaged and demagnified with a typical dimension of 2 μm onto the sample. To reach a field of view that covers the whole sample, in the range of 10×10–16×16 μm^2, the condenser is mounted on a x-y scanner and can be used at variable frequencies for adjusting exposure time. Two Ni FZP lenses, made also by Xradia Inc., are available. They are characterized by outermost zone widths of 40 and 25 nm (named hereafter, ZP40 & ZP25), 937 and 1,500 zones, that give 2.52 and 1.57 mm theoretical focal lengths, respectively, at 520 eV energy of illumination.

2.2. Apparent transfer function

Linear systems are characterized in Fourier domain by a transfer function. In optical systems, the concrete magnitude that establishes the relationship between input and output varies: *amplitude*

Biomedical Optics EXPRESS

transfer function for electric field amplitude in coherent systems and *optical transfer function* for intensity in totally incoherent systems [29]. Partially coherent systems are not linear neither in amplitude nor in intensity [28, 30]. In these systems, the *apparent transfer function* (ATF) has been introduced to accurately predict the system response [31]. ATF is defined as:

$$\mathcal{H}_A(\mathbf{f_x}) = \frac{\tilde{I}_{out}(\mathbf{f_x})}{\tilde{I}_{in}(\mathbf{f_x})}, \tag{1}$$

where $\mathbf{f_x} = (f_x, f_y)$ represents the frequency variable, $\tilde{I}_{in}(\mathbf{f_x})$ and $\tilde{I}_{out}(\mathbf{f_x})$ are the Fourier transforms of the input and output intensity distributions of a test pattern, respectively. In this work we have experimentally calculated the ATF using an approach we had previously introduced in [32]. This approach, in a nutshell, requires a Siemens star as test pattern from which a rotationally averaged ATF is obtained.

2.3. Apparent point spread function

Another magnitude used to characterize optical systems is the impulse response in spatial domain. This magnitude is known as point spread function for pure coherent or incoherent systems. For partially coherent systems we will refer to it as *apparent point spread function* (APSF), defined as

$$h_A(\mathbf{x}) = \mathcal{F}^{-1}\left\{\mathcal{H}_A(\mathbf{f_x})\right\}, \tag{2}$$

where $\mathcal{F}^{-1}$ denotes the inverse *Fourier* transform operation in the plane (f_x, f_y).

One of the advantages of the APSF over the ATF is that the former can be used to directly calculate the optical resolution and the DOF for partially coherent systems. Unfortunately, the experimental ATF measurement does not include the phase information and, therefore, the information required to fully recover the APSF is not available [32]. We define here the *pseudo-apparent point spread function* (PAPSF) where the phase content is removed:

$$h_{PA}(\mathbf{x}) = \mathcal{F}^{-1}\left\{|\mathcal{H}_A(\mathbf{f_x})|\right\}. \tag{3}$$

This new function, as we show in the next subsections, can be used to compute the optical resolution and the DOF.

2.4. Rayleigh resolution criterion

In optics, resolution is usually measured according to Rayleigh criterion. This value is defined for totally incoherent illumination as the distance where the first minimum of the Airy intensity pattern of one source point coincides with the maximum of another. Its theoretical expression is $\delta = \frac{0.61\lambda}{NA_O}$, where λ is the wavelength of the illumination and NA_O is the numerical aperture of the objective lens [29]. In the case of partially coherent illumination, defined by the ratio between numerical apertures of condenser and objective lenses $m = \frac{NA_C}{NA_O} < 1$, there is no closed form and numerical calculations must be done [33]. However, we note that the resolution definition for incoherent illumination can also be inversely applied to an APSF profile to calculate the *critical resolution* of an optical system: at the midpoint in the intensity profile addition between two source points separated by Rayleigh resolution distance δ there is an intensity decay from 100% of its maximum to 73.5 % [28]. Therefore, we can measure the critical resolution as the distance in the APSF profile where the intensity decays to 36.75 % (73.5/2), as one can obtain from the PSF intensity profile of a single source point under totally incoherent illumination.

However, the proposed characterization method does not recover the APSF but the PAPSF, which misses the phase from the ATF profiles. Therefore, to validate the feasibility of using PAPSF profiles instead of APSF ones, we show in Fig. 2 transverse profiles of numerical simulation of both APSF and PAPSF at different values of numerical apertures ratio m, being the transverse spatial units normalized to $\frac{\lambda}{NA_O}$. We see that both profiles, APSF and PAPSF, match

Biomedical Optics EXPRESS

along all x-positions, independently of m. That is, for the in-focus plane the APSF is real and therefore there is not phase modulation.

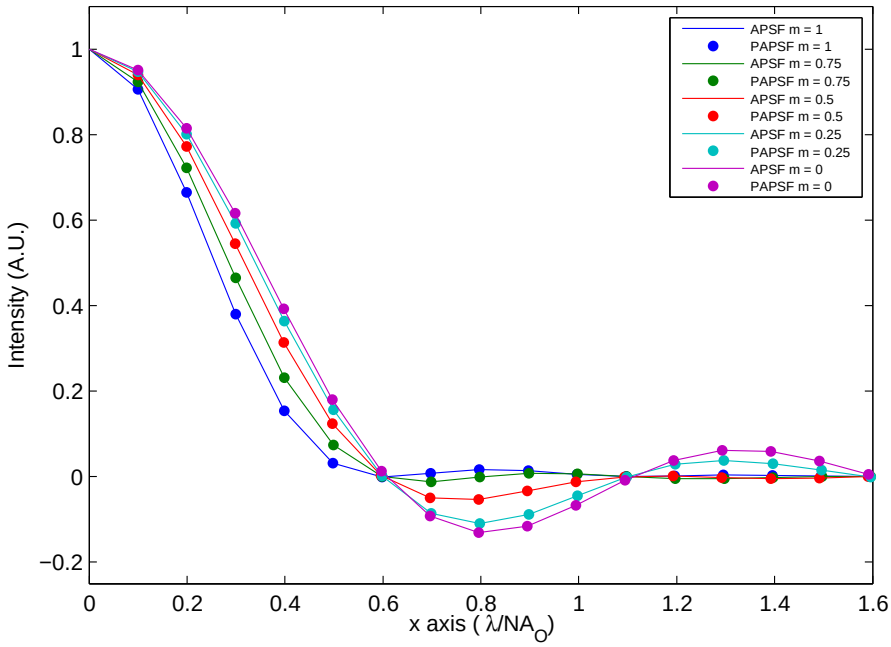

Fig. 2. Transverse profiles of the APSF and PAPSF calculated for different numerical apertures ratio m values. Axial units has been normalized to $\frac{\lambda}{NA_O}$.

2.5. Depth of field

Current 3D reconstructions in soft X-ray tomography are implemented by using tomographic standard reconstruction algorithms, which do not consider the 3D PSF of the optical system and assume that the whole sample is in focus. Therefore, for a proper evaluation of the error related to the ratio between specimen thickness and DOF, it is important to quantify this latter magnitude.

The depth of field is defined as the distance along the optical axis around the best focusing plane where the axial intensity of the PSF decays to 80 % and, as Rayleigh resolution, the analytical expression we find in the literature, $\Delta z = \frac{\lambda}{NA_O^2}$, is only defined for totally incoherent illumination [28, 34]. Therefore, akin to the critical resolution measurement, the DOF can be experimentally calculated from the APSF along the optical axis.

In the previous subsection, we showed a perfect match between PAPSF and APSF profiles for in-focus planes (see Fig. 2), which does not have to occur at every unfocused plane. Thus, to validate the DOF obtained from PAPSF, we show in Fig. 3 the numerical simulation of the profile along the optical axis (that is, at different defocus) of both APSF and PAPSF for different values of numerical apertures ratio m. We note that, for those intensity values used for estimating the DOF (intensities greater than 80 %), both APSF and PAPSF profiles practically match. The discrepancy increases with defocus because the ATF phase component is not negligible for medium and large defoci.

Calculations show that the DOF obtained from the PAPSF introduces an error lower than 1 %

Biomedical Optics EXPRESS

for $m \geq 0.25$, which increases to 6% for the totally coherent case ($m = 0$). We also note that, as m decreases, the DOF clearly varies, which allows to assess that the theoretical definition of the DOF is only valid for a totally incoherent illumination.

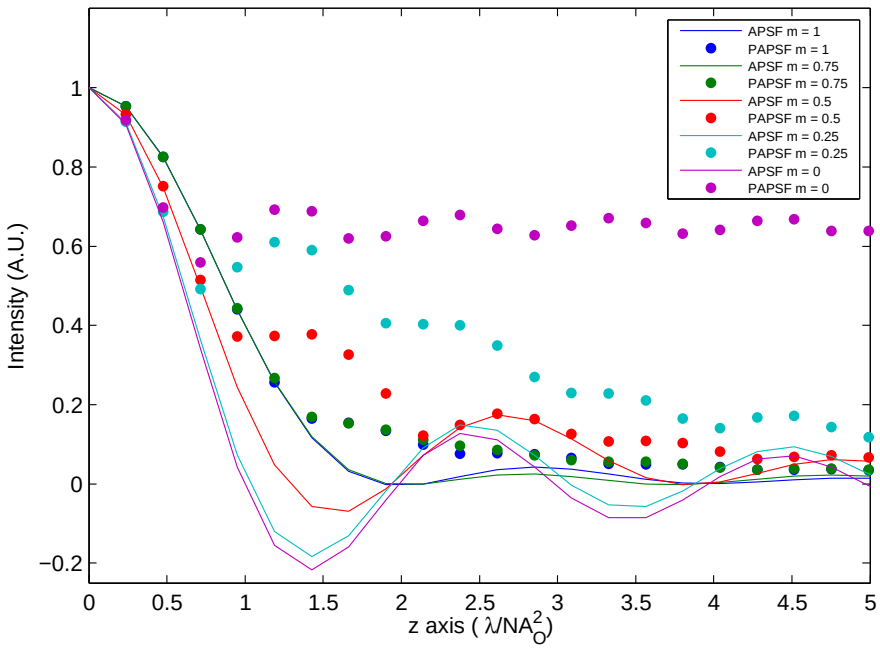

Fig. 3. Axial profiles of the APSF and PAPSF calculated for different numerical apertures ratio m values. Axial units has been normalized to $\frac{\lambda}{NA_O^2}$.

2.6. Deconvolution

Even if we assume that the specimen is fully in focus, images are blurred by the microscope impulse response. Consequently, reconstruction will improve if standard deconvolution is applied to experimental data. The image formation process within this assumption, known as the X-ray transform, is described as [35]:

$$I_s(\mathbf{x}) = \left[I_0(\mathbf{x}) \mathrm{e}^{-\int_{z_0}^{z_s} \mu(\mathbf{x},z)\mathrm{d}z} \right] \otimes h_A(\mathbf{x}), \tag{4}$$

where $\mathbf{x} = (x, y)$, $I_0(\mathbf{x})$ and $I_s(\mathbf{x})$ are the projections acquired without and with the sample (that is, the flatfield reference and projection images), respectively; $\mu(\mathbf{x}, z)$ is the volume that describes the 3D distribution of the sample absorption coefficients, with $\mu > 0 \; \forall \; z \in [z_0, z_S]$ and $\otimes$ denotes the convolution operation in ($\mathbf{x}$). The inversion of Eq. (4) has already been proved to recover the information of the standard projection [35]:

$$\int_{z_0}^{z_s} \mu(\mathbf{x}, z)\mathrm{d}z = -\ln \left[\frac{I_s(\mathbf{x}) \otimes h_A^{-1}(\mathbf{x})}{I_0(\mathbf{x}) \otimes h_A^{-1}(\mathbf{x})} \right], \tag{5}$$

where $h_A^{-1}(\mathbf{x})$, defined as $h_A(\mathbf{x}) \otimes h_A^{-1}(\mathbf{x}) = \delta(\mathbf{x})$, is the deconvolution kernel. Equation (5) shows that when applying a deconvolution operation on both projection and flatfield images a better

Biomedical Optics EXPRESS

estimation of the ideal projections is obtained. Furthermore, as flatfield projections of the background illumination pattern are slowly varying along x-y plane, the flatfield deconvolution can be ignored.

To properly deconvolve the image projections, we must consider the quantum nature of the photons when they interact with detection devices. Wiener filtering has been proved to be an efficient implementation of the deconvolution process under the presence of shot noise [36]. Thus, the estimated projection is calculated in Fourier space as

$$\tilde{I}_s^e(\mathbf{f_x}) = W(\mathbf{f_x})\tilde{I}_s(\mathbf{f_x}), \tag{6}$$

where $\tilde{I}_s^e(\mathbf{f_x})$ and $\tilde{I}_s(\mathbf{f_x})$ are the Fourier transforms of the estimated and true image projections, respectively, and $W(\mathbf{f_x})$ is the Wiener estimator defined as

$$W(\mathbf{f_x}) = \frac{\mathcal{H}_A^*(\mathbf{f_x})}{|\mathcal{H}_A(\mathbf{f_x})|^2 + \frac{S_n(\mathbf{f_x})}{S_I(\mathbf{f_x})}}, \tag{7}$$

where $S_n(\mathbf{f_x}) = \mathcal{F}\{\Phi_N(\mathbf{x})\}$ and $S_I(\mathbf{f_x}) = \mathcal{F}\left\{\Phi_{\tilde{I}_s}(\mathbf{x})\right\}$ are the power spectral densities of the noise and true projections, respectively, calculated as the Fourier transform of the autocorrelation function of the noise, N, or signal, $\tilde{I}_s$, images and their ratio is the SNR. In practice, as photon noise is statistically independent (i.e. white noise), the SNR can be easily obtained as the ratio between the variance of the background illumination (as instance, from the flatfield projections) and estimated projections.

3. Results

In this work, we show the characteristic ATF and PAPSF experimental profiles of the Mistral microscope. In Fig. 4(a) we show the experimentally measured ATF for both ZP40 and ZP25. The profiles for both lenses are similar, being the cut-off frequency of ZP25 greater than ZP40's, as expected by theory. ATF coefficients when f_x approaches zero are not achievable by the measurement method based on the Siemens star test pattern. However, as the normalization in the method recovers the modulation without considering any energy lost, ATF should reach 1 at $f_x = 0$.

To calculate the PAPSF distributions, the 1D profiles depicted in Fig. 4(a) are extrapolated for low frequencies. After that, a 2D-ATF is created assuming rotational symmetry and, finally, Eq. (3) is applied. In Fig. 4(b) the PAPSF profiles for the in-focus plane are shown, being ZP25 profile clearly tighter than ZP40. From these PAPSF profiles, we have obtained critical resolution values of 61.9 and 51.8 nm for the ZP40 and ZP25 lenses, respectively, whereas theoretical resolution values for both ZP40 and ZP25 ideal lenses are 48.8 and 30.5 nm, respectively, in the totally incoherent case.

From the PAPSF intensity along the optical axis we obtain the axial profiles plotted in Fig. 4(c). We clearly note the tighter peak corresponding to ZP25, consequence of the smaller DOF. We have obtained DOF values of 3.3 and 1.6 μm for the ZP40 and ZP25 lenses respectively, whereas theoretical values for both ZP40 and ZP25 ideal lenses are 2.69 and 1.05 μm respectively, in the totally incoherent case. Again, experimental DOF values differ from theoretical ones, enlarged probably by a smaller numerical aperture ratio m than expected, in both cases.

3.1. Tomographic reconstruction

We have used the experimental PAPSF profiles shown in Fig. 4(b) to implement our deblurring Wiener filter. In the following, we show the result of deblurring two experimental datasets, one acquired with each of the two FZPs. The first reconstructed volume by SXT was obtained on a *Scenedesmus* cells sample using ZP40 (*Scenedesmus* is a phototrophic microorganism isolated

Biomedical Optics EXPRESS

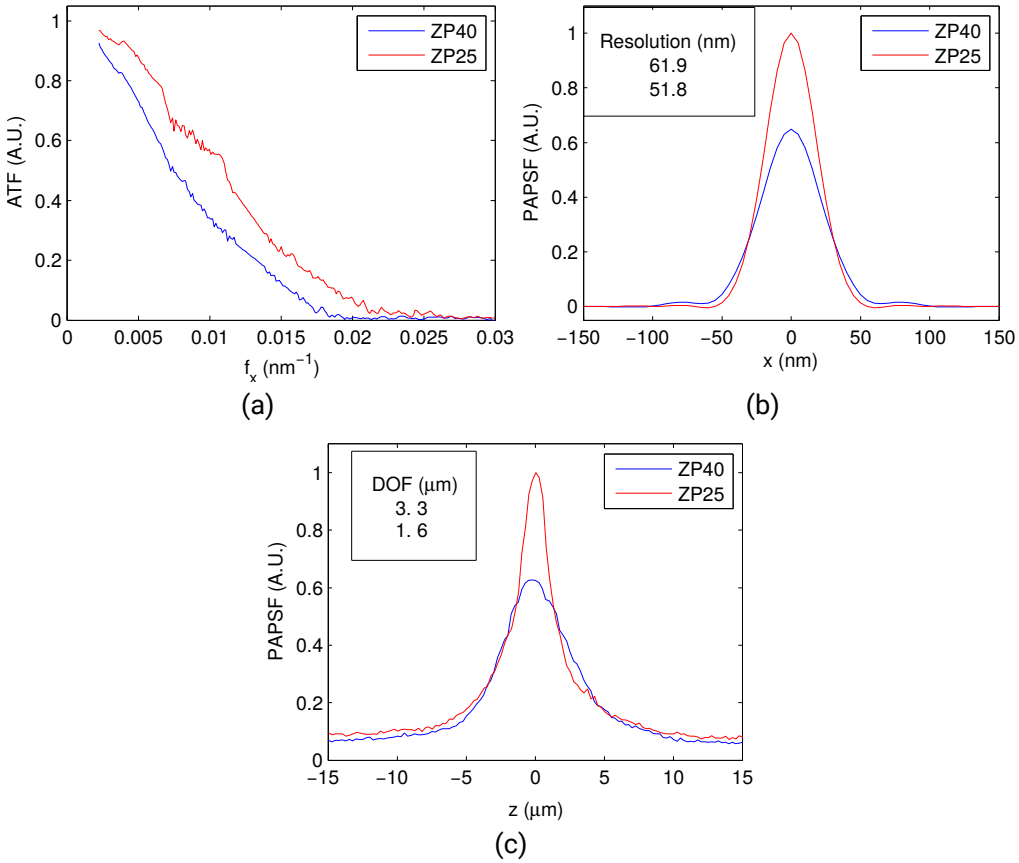

Fig. 4. Experimental characterization of the Mistral microscope when using: ZP40, 937 zones, 2.52 mm theoretical focal length (blue); and ZP25, 1,500 zones, 1.57 mm theoretical focal length (red). Profiles have been calculated for 520 eV. (a) Apparent transfer function profiles; (b) Pseudo apparent transfer function profile calculated at in-focus plane. Applying Rayleigh criteria results in critical resolution values of 61.9 and 51.8 nm for ZP40 and ZP25 lenses, respectively; (c) Axial apparent transfer function profiles. Experimental DOF are 3.3 and 1.6 µm for ZP40 and ZP25, respectively.

from Ebro delta (Spain) microbial mats in 2009), while the second reconstructed volume case, Huh-7 cells (human hepatoma cell line), was collected using ZP25. Both datasets were acquired at 520 eV photon energy. Collection geometry was single-tilt axis in the range [-60°, 70°] in 1° steps, with variation of exposure time between 2 and 3 s and pixel size of 13 nm for ZP40; and in the range [-65°, 65°], using 1° steps, exposure time between 2 and 3 s and 11.3 nm pixel size for ZP25. Comparing the local variance in these projections to the variance of the flatfield image projections, we obtained a value of $SNR \approx 20$ to be used in the Wiener filter.

We show the results for the reconstructed tomograms using ZP40 and ZP25 in Figs. 5 and 6, respectively. We compared an x-z slice (normal to tilt axis) where no deconvolution has been applied (Figs. 5(a) and 6(a)) to the same x-z slice enhanced by deconvolution (Figs. 5(e) and 6(e)). We also compared distinct x-y slices at the same z positions from the standard reconstruction (Figures 5(b-d) and 6(b-d)) with reconstructed slices from deconvolved tomograms (Figures 5(f-h) and 6(f-h)). Clearly, details are enhanced by a contrast increase in the deconvolved case, as shown in the profiles depicted in Figs. 5(i) and 6(i). We note in the case of *Scenedesmus* that details in the slice at $z = 2$ µm, out of the DOF, are also enhanced.

Biomedical Optics EXPRESS

For quantitative assessment of the deconvolution improvement, since the Fourier ring correlation is invariant against deconvolution [37], we applied a blind image quality assessment (AQI) [38] to evaluate absolute image quality without a reference. We analyzed these AQI measures at the different z planes when FZPs ZP40 and ZP25 are used in Figs. 5(j) and 6(j), respectively. AQI shows that, in all the slices, the quality of the images has been increased after the application of the tailored deconvolution.

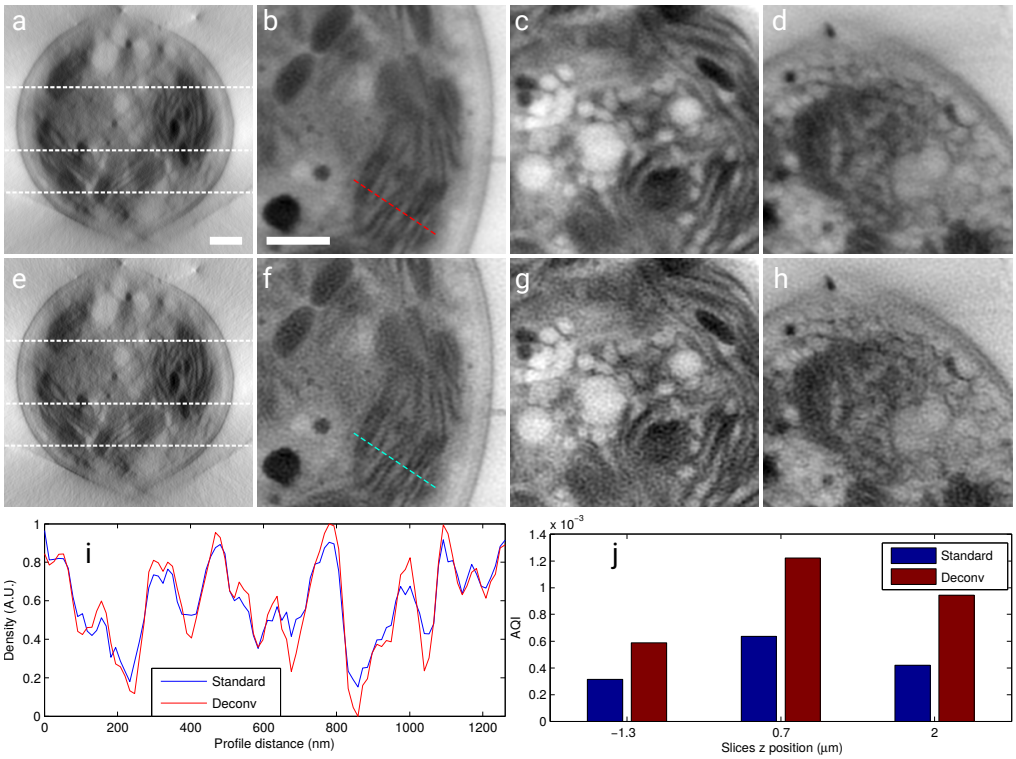

Fig. 5. Comparison of *Scenedesmus* cells tomograms obtained using ZP40. The first row shows standard tomographic results (non-deconvolved), while the second row presents the reconstruction from deconvolved tilt series tomogram. (a, e) Sections perpendicular to the tilt axis where three dashed lines are drawn, corresponding to slices in x-y plane at different distances in z: (b, f) z=-1.3 µm, (c, g) z=0.7 µm and (d, h) z=2 µm. Scale bars = 1 µm; (i) Density profile along the dashed red line marked in (b) compared to the same profile, dashed blue line, in (f); (j) Anisotropic quality index (AQI) comparison of slice pairs (b,f), (c,g) and (d,h). In all the cases the visibility of the slices is enhanced in the case when deconvolution is applied.

Biomedical Optics EXPRESS

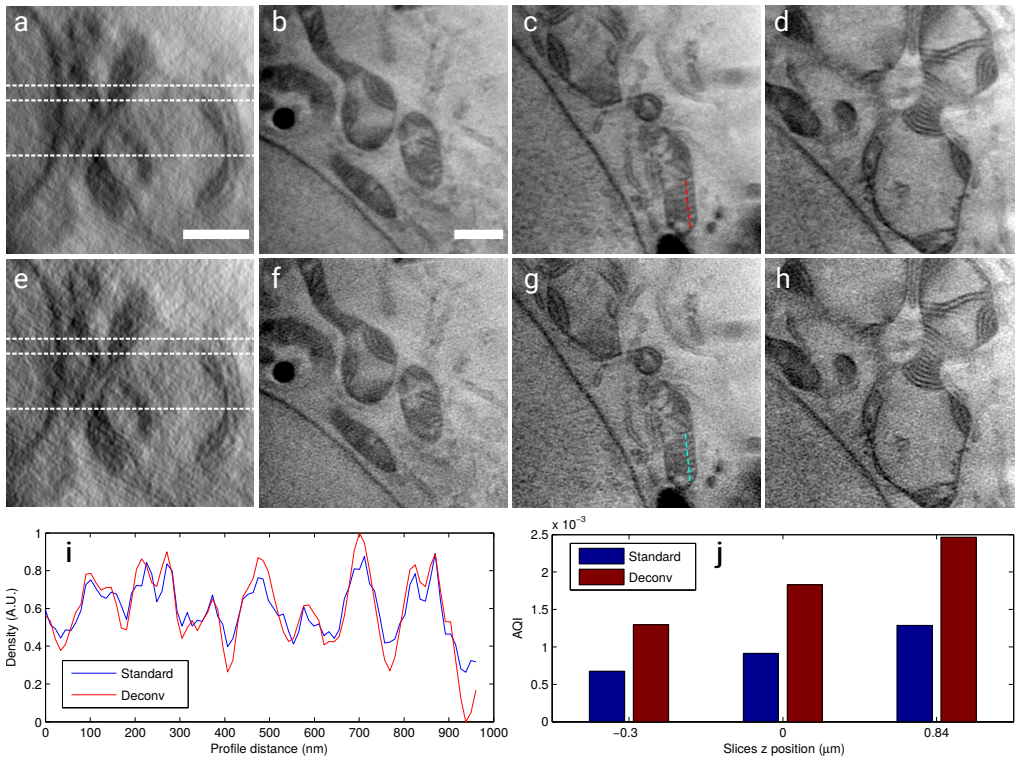

Fig. 6. Comparison of Huh-7 cells tomograms obtained using ZP25. The first row shows standard tomographic results (non-deconvolved), while the second row presents the reconstruction from deconvolved tilt series tomogram. (a, e) Sections perpendicular to the tilt axis where three dashed lines are drawn, corresponding to slices in x-y plane at different distances in z: (b, f) z=-0.3 μm, (c, g) z=0 μm and (d, h) z=0.84 μm. Scale bars = 1 μm; (i) Density profile along the dashed red line marked in (c) compared to the same profile, dashed blue line, in (g); Anisotropic quality index (AQI) comparison of slice pairs (b,f), (c,g) and (d,h). In all the cases the visibility of the slices is enhanced in the case when deconvolution is applied.

4. Conclusions

In this work, we have used experimental measures of the ATF at different defocus to calculate the 3D PAPSF. This distribution allows the estimation of the Rayleigh resolution and the depth of field of the Mistral microscope. We have also designed a Wiener filter which, once applied to experimental image projections, results in an increase of quality in the final reconstructed tomograms.

Our experimental estimation of the Mistral microscope DOF and resolution differ from the design specifications and, although the condenser manufacturing fits the design parameters, the effective illumination pattern provided by the capillary leads to a lower effective numerical aperture with respects to the theoretical one. Therefore, when ZP40 is used the microscope response matches the one of a partially coherent system instead of an incoherent one, while in the case of ZP25 the response corresponds to a more coherent system than design.

Biomedical Optics EXPRESS

Author contributions

JO, EP and JMC designed research; EP performed experiments; JO performed most data analysis with the support of EP, AJP, COSS, and RM; JO designed software tools for data analysis; We have used datasets from AJP and LM as examples of the effect of the deconvolution; JO, JMC, COSS and RM supervised the mathematics; data was acquired in the Mistral beamline at the ALBA synchrotron; JO, JMC and EP prepared the manuscript. All authors reviewed the manuscript.

Funding

Ministerio de Economía y Competitividad (MINECO) (AIC-A-2011-0638, BIO2013-44647-R, BFU2013-41249-P, BIO2016-76400-R, BFU2016-74868-P); Madrid regional government (S2010/BMD-2305); The European Union BioStruct-X Project (283570).

Acknowledgements

All the images in this work were acquired at Mistral beamline at ALBA Synchrotron. We thank ALBA staff, especially Marc Rosanes. We thank J.J. Conesa and F.J. Chichón for figure suggestions.